Multiscale modelling of lubrication between rough surfaces: Application to gas lubrication

Noël Brunetière, Arthur Francisco

Received: Added at production | Revised: Added at production | Accepted: Added at production

DOI: xxx/xxxx

ARTICLE TYPE

Multiscale modeling of lubrication between rough surfaces: Application to gas lubrication.

Noël Brunetière*[1] | Arthur Francisco[2]

[1]Institut Pprime, CNRS, Université de Poitiers, ENSMA, Poitiers, France
[2]Institut Pprime, CNRS, Université de Poitiers, ENSMA, Angoulême, France

Correspondence
*Corresponding author Noël Brunetière, Institut Pprime, Dept. GMSC, CNRS - Université de Poitiers - ENSMA, SP2MI, 11 Bd Marie et Pierre Curie, 86360 Chasseneuil du Poitou - France. Email: noel.brunetiere@univ-poitiers.fr

Present Address
This is sample for present address text this is sample for present address text

Summary

Calculating the flow of a film of lubricant between rough surfaces by solving the Reynolds equation requires a very fine mesh to capture the details of the topography and is thus very time consuming. In the present paper, a multiscale method is proposed. The domain is divided into an appropriate number of subdomains on which deterministic simulations are performed. The results of this microscale solution are coupled at the macroscale by employing a macromesh on which a mass flow balance is implemented. This method has already been successfully applied to liquid lubrication and is extended to gas lubrication. A significant reduction in computation time is obtained compared to a fully deterministic solution. The calculation of the load is also accurate.

KEYWORDS:
Gas lubrication, Surface roughness, Finite element method, Multiscale.

1 | INTRODUCTION

Gas lubricated systems such as air bearings have some advantages, such as their eco-friendly lubricant, low viscosity variations with temperature, and low friction, making their use very common in high precision or high speed applications[1]. Gas lubricated bearings are usually designed to work with a sufficiently high film thickness to avoid asperity contact. However, in some situations, the surface roughness can affect the flow of the lubricating gas. Typical examples are very low film thickness applications, such as hard drive disk sliders[2,3], start-up and shut-down of bearings[4,5] or spiral groove gas seals[6] and static and mechanical seals[7,8]. In addition to the effect of roughness, a low film thickness is accompanied by the rarefaction of the gas between the surfaces[9]. This happens when the mean free path of the gas is of the order of magnitude of the thickness of the film. This leads to slipping of the gas on the surface. This point will not be addressed in this paper.

In the early 80's, several authors proposed solutions to include the effect of roughness in the Reynolds equation for gas lubrication. First, White[10] proposed an asymptotic solution for the case of high values of the compressibility number, Λ, corresponding to dominant shear flow in the contact. In this case, the pressure is proportional to the inverse of the film thickness. A few years later, Tonder[11] extended his averaging technique developed for liquid lubrication of striated surfaces to gas lubrication. In the case of high Λ, Tonder obtained a pressure solution different from the one given by White. Greengard[12], by analyzing the relative magnitude of Λ and β, the ratio of the domain length to the roughness length scale, showed that both solutions are verified but in different relative ranges of Λ and β. The pioneering works of White and Tonder have been improved over the years. A review can be found in[13].

A second family of approaches is based on the flow factors introduced by Patir and Cheng[14,15] for incompressible lubricants between rough surfaces. This method consists in applying correcting factors to the Reynolds equation, and has been extended to gas lubrication[16]. Since the flow factors can be numerically calculated, this method can consider different types of roughness

as well as a rarefied flow. The homogenization method is also popular to deal with roughness in liquid lubricated systems [17] and was extended to gas lubrication [18].

All these averaging methods have the advantage of considering roughness with a very coarse discretization, but, however, are unable to provide details of the pressure distribution. Some deterministic approaches based on advanced numerical methods and supercomputers were proposed in the 90's and more recently, but are limited to a small number of roughness length scales, that is to say, small domains [19,2,20,21].

The present paper applies a finite element multiscale method [22] to gas lubrication. The domain is divided into a suitable number of subdomains, on which deterministic simulations are performed. The results of these microscale simulations are coupled at the macroscale level by employing a macromesh on which a mass flow balance is implemented. This method offers the advantage of low computation time yet reasonable accuracy. For quite large meshes, it provides details of the pressure distribution over the whole domain. In the present paper, the effect of the number of subdomains, the compressibility number, and the ratio of the roughness correlation length to the domain size (i.e., β^{-1}) will be analyzed.

2 | MATERIALS AND METHODS

2.1 | Configuration, equations and assumptions

The configuration of the studied problem is presented in Fig. 1. A smooth plate normal to $\vec{z}$ is sliding at speed V in the $\vec{x}$ direction. A rough plate at rest and of lateral size L is placed at an average distance of h_0 from the moving plate. The height of the roughness is described by the standard deviation Sq. The roughness is, in this study, isotropic and its correlation length is Sal (definition according to ISO 25178). The gap between the two plates is filled with an ideal gas. The pressure along the boundaries is equal to p_a.

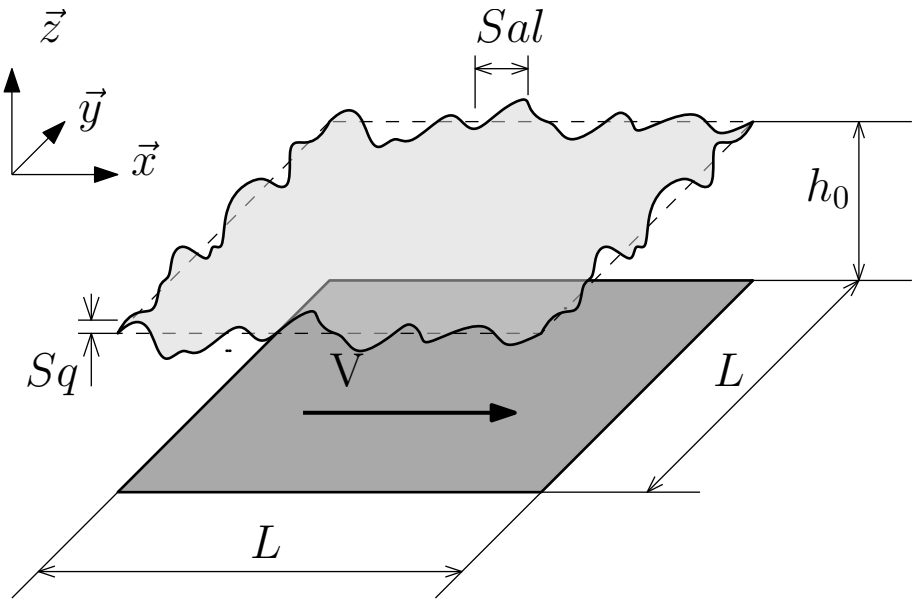

FIGURE 1 Configuration of the problem.

For this particular study, the following additional assumptions are used:

1. The problem is stationnary;
2. The flow is isothermal;
3. The gas film is continuous (no rarefaction effect);
4. There is no asperity contact;

5. The thickness of the gas film is small compared to the lateral size of the surface, i.e., $h_0 \ll L$;
6. The roughness slope is small (Reynolds type roughness[23]) $h_0 < \frac{Sal}{5}$.

In the case of an ideal gas, the relation between the pressure p, density ρ and temperature T is

$$p = \rho r_g T \tag{1}$$

where r_g is the gas constant. Based on assumption 2, the temperature T is uniform and equal to the ambient temperature T_a. The density is thus proportional to the pressure: $\rho \propto p$.

Assumption 3 can be verified by using the Knudsen number, which must be small when compared to 1. It is the ratio of the mean free path in the gas to the thickness of the gas film, and for an ideal gas can be expressed by[9]

$$Kn = \frac{\mu\sqrt{2\pi r_g T}}{2ph_0} \tag{2}$$

where μ is the fluid dynamic viscosity.

Under all these assumptions, the gas flow in the gap between the surfaces can be described by the Reynolds equation:

$$\frac{\partial}{\partial x}\left(\frac{\rho h^3}{12\mu}\frac{\partial p}{\partial x}\right) + \frac{\partial}{\partial y}\left(\frac{\rho h^3}{12\mu}\frac{\partial p}{\partial y}\right) = \frac{V}{2}\frac{\partial \rho h}{\partial x} \tag{3}$$

To highlight the relative importance of the different terms of the equation, it is necessary to introduce non-dimensional parameters:

$$\begin{aligned} p &= \bar{p}p_a \\ \rho &= \bar{\rho}\frac{p_a}{r_g T_a} \\ h &= \bar{h}h_0 \\ x &= \bar{x}L \\ y &= \bar{y}L \end{aligned} \tag{4}$$

The Reynolds equation can be written in a dimensionless form:

$$\frac{\partial}{\partial \bar{x}}\left(\bar{\rho}\bar{h}^3\frac{\partial \bar{p}}{\partial \bar{x}}\right) + \frac{\partial}{\partial \bar{y}}\left(\bar{\rho}\bar{h}^3\frac{\partial \bar{p}}{\partial \bar{y}}\right) = \Lambda\frac{\partial \bar{\rho}\bar{h}}{\partial \bar{x}} \tag{5}$$

The magnitude of the right hand side is controlled by the compressibility number:

$$\Lambda = \frac{6\mu V L}{P_a h_0^2} \tag{6}$$

When $\Lambda \gg 1$, this term is dominant, and thus the density and the pressure are proportional to the inverse of the film thickness $\bar{p} \propto \bar{h}^{-1}$. This is the solution proposed by White[10]. This limit relation highlights that the pressure wavelength and the surface wavelength are strongly linked.

The parameters used in the present study are detailed in Table 1. The simulations will be performed with the numerically generated surface presented in Fig. 2. To analyze the impact of the wavelength of the surface roughness, five additional surfaces with different correlation lengths will be used (see Fig. 3). These surfaces have been used in a previous paper[22]. Due to the very low film thickness used in this paper, the Knudsen number $Kn = 0.158$ is not really small compared to 1. However, it was decided by the authors to ignore its impact to focus on the effect of the roughness on the solution of the Reynolds equation with a multiscale approach. Note that the effect of rarefaction can be easily introduced into the model using the method of Fukui and Kaneto[9].

TABLE 1 Operating conditions and rough surfaces parameters.

Parameter	**Value (nominal value in bold)**
Surrounding pressure p_a	0.1 MPa
Gas viscosity μ	1.8×10^{-5} Pa.s
Domain size L	2 mm
Average film thickness h_0	0.4 μm
Sliding speed V	0.1–300 m.s^{-1}
Compressiblity number Λ	1.35 – 4050
Roughness height Sq	0.1 μm
Roughness correlation length Sal	**14**–248 μm
Roughness correlation lengthes ratio Str	$\simeq 1$
Number of points n	2049×2049
Roughness height to film thickness ratio Sq/h_0	0.25
Roughness correlation length to domain size ratio Sal/L	**0.007** – 0.124
Knudsen number Kn	0.158

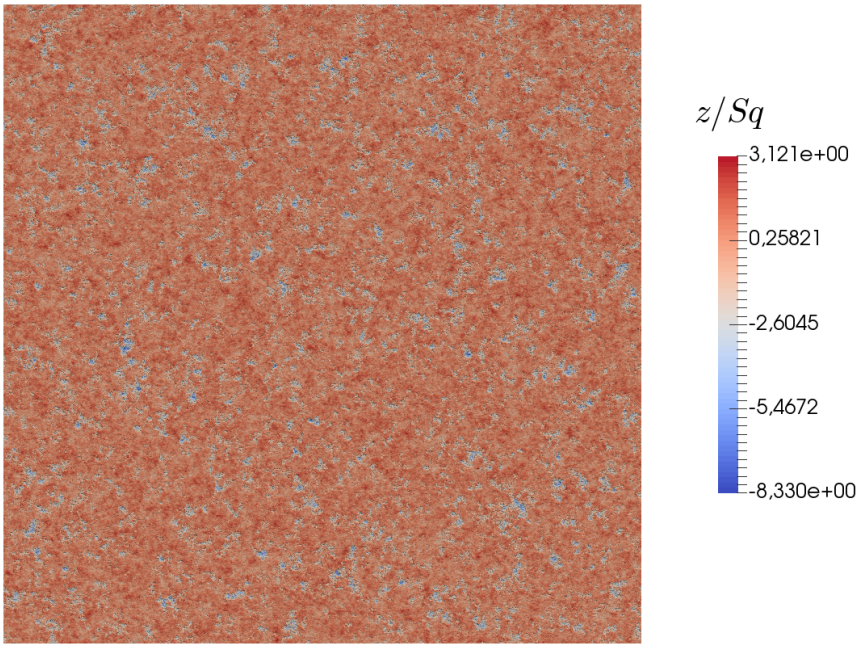

FIGURE 2 Reference rough surface.

2.2 | Finite element solution

The Reynolds equation 3 is solved using the finite element method as described in our previous paper[22]. There are however a few differences. The problem is nonlinear due to the compressibility of the fluid, and an iterative solving process is needed. Secondly, due to the pressure–density relation, there is a convective type term in the right hand side of Eq. 3. An upwind scheme is applied, as described in[24].

The domain is divided into n_e contiguous quadrangular elements. The n nodes where the pressure is unknown are located at the corners of these elements. An equation is needed for each unknown. It is obtained by multiplying the Reynolds equation by

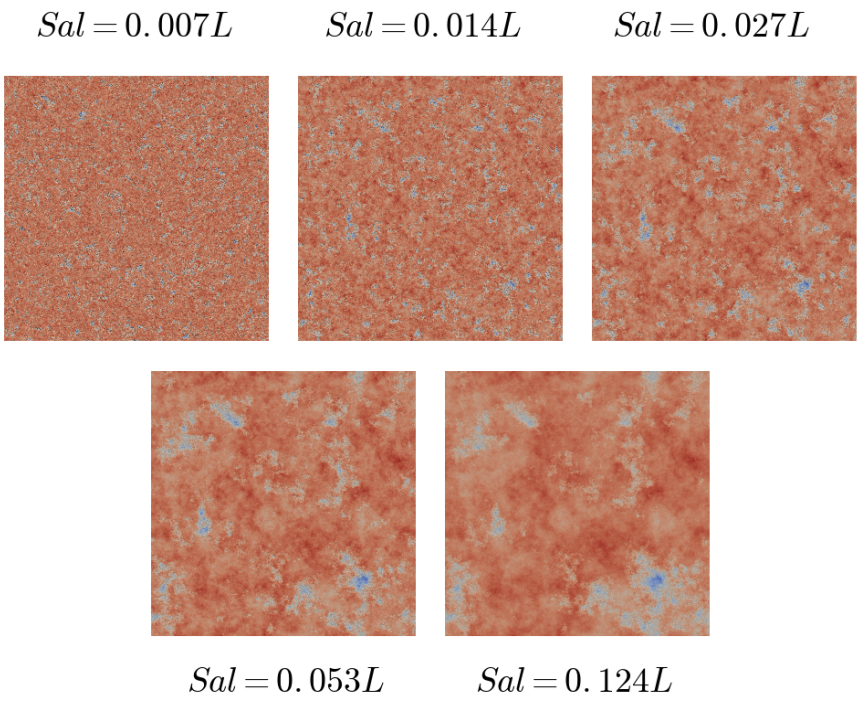

FIGURE 3 Different rough surfaces.

a weight function and integrating over the whole domain Ω. Here, for each node i, the shape function N_i is used as the weight function. A residual R_i is obtained:

$$R_i = \int_\Omega N_i \left[\frac{\partial}{\partial x}\left(\frac{\rho h^3}{12\mu}\frac{\partial p}{\partial x}\right) + \frac{\partial}{\partial y}\left(\frac{\rho h^3}{12\mu}\frac{\partial p}{\partial y}\right) - \frac{V}{2}\frac{\partial \rho h}{\partial x}\right] \mathrm{d}\Omega \tag{7}$$

In order to reduce the order of the derivatives, an integration by parts is performed. The weak integral form is thus obtained:

$$\begin{aligned} R_i = &- \int_\Omega \left[\frac{\partial N_i}{\partial x}\frac{\rho h^3}{12\mu}\frac{\partial p}{\partial x} + \frac{\partial N_i}{\partial y}\frac{\rho h^3}{12\mu}\frac{\partial p}{\partial y} - \frac{\partial N_i}{\partial x}\frac{V}{2}\rho h\right] \mathrm{d}\Omega \\ &+ \underbrace{\int_\Gamma N_i \left[\frac{\rho h^3}{12\mu}\frac{\partial p}{\partial x}n_x + \frac{\rho h^3}{12\mu}\frac{\partial p}{\partial y}n_y - \frac{V}{2}\rho h n_x\right] \mathrm{d}\Gamma}_{\text{Flow rate along the boundary } \Gamma} \end{aligned} \tag{8}$$

In this formulation, a contour integral appears. It corresponds to the mass flow rate weighted by the shape function N_i along the boundary Γ of the domain. This term vanishes except for the shape function of nodes located on the boundary. As the pressure is known and equal to p_a along the boundary, the residual for nodes on the boundary is not calculated. Thus the contour term is never calculated and will be ignored in the next equations.

The solving process consists in finding pressure nodal values p_i that nullify all the residuals R_i (Eq. 8). Since the problem is nonlinear, it is more efficient to use the Newton–Raphson procedure. The system of equations is obtained by differentiation of the residuals R_i with respect to the p_j:

$$\frac{\partial R_i}{\partial p_j}\delta p_j = -R_i \tag{9}$$

The derivative can be expressed as

$$\frac{\partial R_i}{\partial p_j} = -\int_\Omega \left[\frac{\partial N_i}{\partial x}\frac{\rho h^3}{12\mu}\frac{\partial N_j}{\partial x} + \frac{\partial N_i}{\partial y}\frac{\rho h^3}{12\mu}\frac{\partial N_j}{\partial y}\right] \mathrm{d}\Omega$$
$$-\int_\Omega \left[\frac{\partial N_i}{\partial x}\frac{N_j K_j h^3}{12\mu}\frac{\partial p}{\partial x} + \frac{\partial N_i}{\partial y}\frac{N_j k_j h^3}{12\mu}\frac{\partial p}{\partial y} - \frac{\partial N_i}{\partial x}\frac{V}{2}N_j K_j h\right] \mathrm{d}\Omega \tag{10}$$

where K is the derivative of the fluid density with respect to the pressure. It can be formally expressed by means of the ideal gas law:

$$K = \frac{\partial \rho}{\partial p} = \frac{1}{r_g T} \tag{11}$$

The system of equations is solved by MUMPS[1], which is a multithreaded sparse matrices solver based on the LU decomposition.

2.3 | Multiscale method

The idea of the multiscale method is to discretize the problem at two different scales. The domain Ω is first meshed with a coarse grid containing n_e^t elements. This is the top scale. For simplicity, it is assumed here that all these elements have the same size. It is, however, possible to use elements of different sizes. Each of these top elements is meshed with a fine grid containing n_e^b elements. This is the bottom scale. For the sake of comparison, the size of the bottom grid is the same as the standard finite element approach. Thus the following relation holds.

$$n_e = n_e^t \times n_e^b \tag{12}$$

The pressure distribution from the topscale is applied as boundary conditions for the bottomscale problem. The bottomscale problem is then solved using the previously described standard finite element approach. The pressure distribution at the topscale must be adjusted to ensure mass conservation between the topscale elements. Knowing the pressure distribution at the bottom scale, it is possible to calculate the mass flow rate weighted by the top shape function:

$$Re_i^t = \int_{\Gamma_e^t} N_i^t \underbrace{\left[\frac{\rho h^3}{12\mu}\frac{\partial p}{\partial x}n_x + \frac{\rho h^3}{12\mu}\frac{\partial p}{\partial y}n_y - \frac{V}{2}\rho h n_x\right]}_{\text{Calculated at the bottom-level}} \mathrm{d}\Gamma_e^t \tag{13}$$

By adding the contributions of all the elements, a residual for each node of the top scale is obtained:

$$\sum_{e=1}^{n_e^t} Re_i^t = R_i^t \tag{14}$$

This residual must be zero to ensure mass conservation between the elements. Since the problem is nonlinear, the Newton–Raphson method is applied. The derivatives of the residual are numerically calculated at the bottom scale using a small pressure increment at the boundary of the bottom element. The final system that must be solved to find the top scale pressure is

$$\frac{\partial R_i^t}{\partial p_j^t}\delta p_j^t = -R_i^t. \tag{15}$$

The procedure of the multiscale approach is summarized in Fig. 4. The top scale system of equations is solved by MUMPS. The bottom scale systems are independent and are solved in parallel using the OPEN-MP library. They are solved using the multi-frontal UMFPack[2] solver in its single-threaded version. The multiscale model, called MultiScale Simulation of Tribology (MuSST) is an open-source application written in modern Fortran and available on the Internet[3]. The different solvers used in the model are embedded in an open source Fortran library, MSOLV [4].

[1] http://mumps.enseeiht.fr/
[2] http://faculty.cse.tamu.edu/davis/suitesparse.html
[3] https://tribo-pprime.github.io/MUSST/
[4] https://tribo-pprime.github.io/MSOLV/

The main advantage of the multiscale approach is the reduction in the computation time due to the decrease in the number of operations needed to solve the system ([22]) and the parallel computation. However, the linear pressure distribution along the top scale elements and the boundaries of the bottom scale subdomains induce errors in the final pressure distribution. The computational efficiency as well as the error of the multiscale approach will be analyzed in the next section.

3 | RESULTS

3.1 | Example of the results

In the next section, the multiscale solution is compared to the exact finite element solution, referred to as the deterministic solution. For the multiscale approach, the domain of size L (Fig. 1) is divided into subdomains. The side of each subdomain, i.e., top scale element, has size $\frac{L}{k}$. The number of top scale elements is $n_e^t = k^2$. The number of elements of each bottom scale domain is thus $n_e^b = \frac{n_e}{k^2}$, where n_e is the number of elements of the deterministic solution. In the next section, the results will be presented as a function of k. By definition, $k = 1$ corresponds to the deterministic solution.

Fig. 5 shows examples of the pressure distribution in the gas film when $\Lambda = 1350$. On the left hand side, the pressure distribution obtained with the deterministic solution is presented. Computing the solution took 710 seconds on a 4×2 threads computer. It can be seen that rapid variations of the pressure are observed due to the roughness of the reference surface. On the right hand side, the multiscale solution is presented. It was obtained with $k = 8$, in 194 seconds, which is 3.65 times faster than the deterministic approach. With a top scale mesh that is very coarse, it is not possible to capture the details of the pressure distribution. It gives the main tendencies, which serve as boundary conditions for the bottom scale solution. The pressure distribution on the 8×8 subdomains is presented on the bottom right hand side. The rapid pressure variations observed in the deterministic solution are well captured at the bottom scale. However, some differences are visible, due to the error induced by the linearity of the pressure distribution applied along the boundaries of the subdomains. Increasing k can certainly reduce these differences.

The absolute value of the difference in pressure between the deterministic and bottom scale solutions is presented in Fig. 6 for different k. It can be seen that when $k = 8$, the error is initiated on the boundary of the subdomains and then convected across the macro-element. The transport of the error is due to the high value of Λ making the convective term of the Reynolds equation 5 dominant. When k is increased, the error tends to decrease gradually as the top scale mesh becomes fine enough to capture the main components of the pressure.

3.2 | Performance of the method

Fig. 7 presents the dimensionless load W as a function of the compressibility number Λ for the deterministic approach ($k = 1$) and the multiscale method with different values of k. The dimensionless load is defined by

$$W = \frac{1}{L^2 p_a} \int_0^L \int_0^L p \mathrm{d}x\mathrm{d}y. \tag{16}$$

The generated load in the contacts starts from 1 at low compressibility numbers and then evolves with Λ. As expected, for higher compressibility numbers, the generated load increases. The multiscale approach gives similar results but depending on the number of subdomains per side k, the difference from the exact solution changes. For a larger number of subdomains, the error in the load appears to be smaller. This is in line with the results presented in Fig. 6. For $k = 512$, the solution has been calculated for much higher compressibility number in order to reach the asymptotic solution highlighted in the model of White [10]. These results corresponds to unrealistic sliding speeds.

It is possible to calculate the relative error of the load using the deterministic solution load W_d as a reference. The results are presented in Fig. 8 as a function of the compressibility number divided by k. This number is the compressibility number calculated on a macro-element. Generally speaking, the error is increased when Λ is increased or if the number of subdomains is reduced. It has been possible to determine an upper limit for the error e_u:

$$e_u = \min\left(0.005\frac{\Lambda}{k}, 0.01\right) \tag{17}$$

Is thus possible to adjust the number of subdomains per side k to reach a given accuracy of the load.

The computation time is presented as a function of the compressibility number for the deterministic approach and for the multiscale approach, for different values of k in Fig. 9. Generally speaking, the computation time increases with Λ because the nonlinearity of the problem becomes higher. Although the multiscale method has a linearly increasing computation time, the deterministic model has a sharp increase of the calculational burden at the highest values of Λ. When the multiscale approach is used, the computation time is reduced. This decrease is more pronounced when k is higher and for high Λ. The better computational performance of this method has been discussed extensively in a previous paper[22]. It is mainly due to the lower number of flops and to the use of parallel computation. Note that some small oscillations in the calculation time can be seen. This is due to the fact that the problem is nonlinear, thus it is necessary to define a convergence threshold for the residuals. The number of iterations needed to reach convergence can sometimes increase when the compressibility number has slightly increased, making the total computation time longer.

To have a better illustration of the better computation time provided by the multiscale method, the calculation time was normalized by the computation time of the deterministic approach. The results are presented as a function of k for different values of the compressibility number in Fig. 10. The computation is reduced when k is increased. For the lowest value of Λ, the time reduction factor is about 2.5. For the highest Λ, the computation time can be divided by 16. The method has thus a great advantage when dealing with more severe cases.

3.3 | Effect of the rough surface parameters

The previous results were obtained with the reference surface presented in Fig. 2, for which the correlation length Sal is about 0.007 times the domain size L. To highlight the impact of the asperity lateral size, several surfaces with ratios $\frac{Sal}{L}$ varying from 0.007 to 0.124 were used (see Fig. 3). This number is equivalent to β^{-1}, where β is the parameter used by Tonder[11] and Greengard[12]. For these cases, the compressibility number was set to $\Lambda = 1350$.

The pressure distribution obtained with the deterministic approach for the six different surfaces is presented in Fig. 11. Increasing the correlation length of the surface roughness obviously increases the lateral size of the pressure spots. Theses cases were simulated with the multiscale approach with k varying from 32 to 512.

The relative error of the load is presented in Fig. 12 as a function of the macro-compressibility for the different surfaces. The general tendency observed is that the error increases with the macro-compressibility number, as previously observed. The curves show some major oscillations, and it is difficult to identify any effect due to the surface correlation length Sal. The upper limit of the error e_u defined by Eq. 17 has been added. The error is well below this upper limit.

Fig. 11 show that the main parameter varying with the surface correlation length is the lateral size of the pressure spikes. Thus we determined the correlation length λ_x of the pressure distribution in the sliding direction and the correlation length λ_y in the perpendicular direction. These values were calculated using the same method as for Sal for surface roughness with the freeware Gwyddion[5]. The errors vs. these two parameters were evaluated by using the values from the deterministic solution: λ_x^d and λ_y^d.

The errors of λ_x and λ_y are presented respectively in Fig. 13 and Fig. 14 as functions of the ratio of the roughness correlation length Sal to the macro-element size $\frac{L}{k}$. Decreasing the size of the subdomains provides better accuracy of the pressure correlation length. It has been shown in Fig. 6 that a small number of subdomains induces errors of the pressure at the edges of the subdomains. The results show that if the correlation length of the surface is increased, the number of subdomains can be reduced. Typically, to maintain the errors of λ_x and λ_y below 0.01, five subdomains per surface correlation length are needed.

4 | DISCUSSION

The results presented in the previous section show that the performance and accuracy of the multiscale method depends on k, Λ, and Sal. Fig. 11 shows that increasing Sal increases the lateral size of the pressure peaks. Fig. 15 shows the pressure distribution obtained with the reference surface at different values of Λ. These results were computed with the deterministic approach. At low values of Λ, very wide pressure peaks are obtained but with low amplitude. When Λ increases, this tendency is inverted: the pressure peaks become narrower and their amplitudes increase.

The correlation length of the pressure distributions has been calculated in the x and y directions for all the operating conditions. The correlation lengths of the pressure distribution are presented in Fig. 16 as a function of $\Lambda \times \frac{Sal}{L}$. The pressure correlation

[5] http://gwyddion.net/

length is normalized by the surface correlation length Sal. The results obtained with the reference surface with varying Λ are presented as well as the results obtained with different surfaces having various values of Sal. The two sets of results give consistent results for the pressure correlation length in the x (sliding) and y directions. This indicates that $\Lambda \times \frac{Sal}{L}$ is the parameter controlling the characteristic wave length or correlation length of the pressure distribution.

At low values of $\Lambda \times \frac{Sal}{L}$, λ_x and λ_y reach a plateau for which they are several times bigger than the surface correlation length. This is typical of what is obtained with incompressible fluids (see our previous paper[22]). When the compressibility number is increased, the right hand side term of the Reynolds equation 5 increases and the pressure starts to be more correlated with h, the film thickness, and thus the surface roughness. The correlation lengths of the pressure decrease. If λ_y decreases continuously to values close to Sal, the correlation length in the sliding direction exhibits a different behavior. When $\Lambda \times \frac{Sal}{L} > 2$, a minimum is reached and then λ_x starts to increase. This rise appears when the right hand side term of Eq. 5 becomes dominant. The Reynolds equation becomes a convective dominated equation. Thus there is a transport of the pressure in the sliding direction, creating a kind of pressure striation. This is clearly visible in Fig. 15 when $\Lambda = 4050$. The last point of the curve was obtained with the surface having $Sal = 0.124L$. It is possible that in this case, the increase of λ_x is limited by the domain size that is of the same order of magnitude as Sal. This can explain the decrease obtained for the last point.

The evolution presented in Fig. 16 is very useful to explain the dependency of the accuracy of the multiscale method on k, on the compressibility number Λ, and on the correlation length of the surface Sal. For the multiscale solution to have good fidelity, it is important that the macro-mesh capture the main features of the pressure distribution. For this, the size of the subdomains must be several times smaller than the pressure correlation length. For the case of an incompressible flow, it has been shown that $\frac{L}{k}$ must be less than $\frac{Sal}{2}$ [22]. Using the fact that $\lambda_y \simeq 20 \times Sal$ (respectively $\lambda_x \simeq 8 \times Sal$) at low compressibility numbers, this means that $\frac{L}{k}$ must be less than $\frac{\lambda_y}{40}$ (respectively $\frac{\lambda_x}{16}$). This rule can be extended up to $\Lambda \times \frac{Sal}{L} = 10$. For higher values, it is more difficult to state because λ_y continues to decrease, meaning that higher k values are needed while, on the other hand, λ_x starts to increase, indicating that lower k values are sufficient. In this situation, it would be interesting to use different values of k for the x and y directions.

5 | CONCLUSION

A multiscale finite element approach was presented and applied to gas lubrication between rough surfaces. The domain is divided into an appropriate number of subdomains on which deterministic simulations are performed. The results of this microscale solution are coupled at the macroscale level thanks to a macro-mesh on which a mass flow balance is imposed. This method offers the advantage of low computation time with reasonable accuracy, giving, even for quite large meshes, the details of the pressure distribution over the whole domain.

The reduction in the computation time depends on the number of subdomains and the value of the compressibility number Λ. The best performance is obtained for the highest number of subdomains (512^2) and the highest value of Λ value (4050, in the present paper). In this case the computation time is reduced by 16.

It was shown that the accuracy of the multiscale method depends on the number of subdomains, the compressibility number Λ, and the correlation length Sal of the rough surface. This is due to the fact that the characteristic wave lengths of the pressure distribution vary significantly with $\Lambda \times \frac{Sal}{L}$. Generally speaking, it is better to have a large number of subdomains. A rule of thumb is to check that $\frac{L}{k} < \frac{\lambda_x}{16}$ or $\frac{L}{k} < \frac{\lambda_y}{40}$ where λ_x and λ_y are the pressure correlation lengths and the number of subdomains is k^2. Their evolution is presented in Fig. 16.

ACKNOWLEDGMENTS

This work pertains to the French government program Investissements dâĂŹAvenir (LABEX INTERACTIFS, reference ANR-11-LABX-0017-01, and EUR INTREE, reference ANR-18-EURE-0010).

Financial disclosure

None reported.

Conflict of interest

The authors declare no potential conflict of interests.

References

1. Al-Bender F. *Air Bearings: Theory, Design and Applications*. John Wiley & Sons . 2021.
2. Crone R, Jhon M, Bushan B, Karis T. Modeling the Flying Characteristics of a Rough Magnetic Head Over a Rough Rigid-Disk Surface. *Journal of Tribology* 1991; 113(4): 739-749. doi: 10.1115/1.2920687
3. Li WL, Weng CI, Hwang CC. Effects of roughness orientations on thin film lubrication of a magnetic recording system. *Journal of Physics D: Applied Physics* 1995; 28(6): 1011.
4. Rudloff L, Arghir M, Bonneau O, Matta P. Experimental analyses of a first generation foil bearing: startup torque and dynamic coefficients. *Journal of engineering for gas turbines and power* 2011; 133(9).
5. Balducchi F, Arghir M, Gauthier R, Renard E. Experimental Analysis of the Start-Up Torque of a Mildly Loaded Foil Thrust Bearing1. *Journal of Tribology* 2013; 135(3). 031702doi: 10.1115/1.4024211
6. Hu S, Huang W, Shi X, Peng Z, Liu X, Wang Y. Evolution of bi-Gaussian surface parameters and sealing performance for a gas face seal under a low-speed condition. *Tribology International* 2018; 120: 317 - 329. doi: https://doi.org/10.1016/j.triboint.2018.01.017
7. Ruan B, Salant RF, Green I. A mixed lubrication model of liquid/gas mechanical face seals. *Tribology transactions* 1997; 40(4): 647–657.
8. Polycarpou AA, Etsion I. A model for the static sealing performance of compliant metallic gas seals including surface roughness and rarefaction effects. *Tribology transactions* 2000; 43(2): 237–244.
9. Fukui S, Kaneko R. Analysis of Ultra-Thin Gas Film Lubrication Based on Linearized Boltzmann Equation : First Report - Derivation of a Generalized Lubrication Equation Including Thermal Crepp Flow. *Journal of Tribology* 1988; 110(2): 253-261.
10. White J. Surface Roughness Effects on the Load Carrying Capacity of Very Thin Compressible Lubricating Films. *Journal of Lubrication Technology* 1980; 102(4): 445-451. doi: 10.1115/1.3251579
11. Tonder K. A Numerical Assessment of the Effect of Striated Roughness on Gas Lubrication. *Journal of Tribology* 1984; 106(3): 315-319. doi: 10.1115/1.3260920
12. Greengard C. Large Bearing Numbers and Stationary Reynolds Roughness. *Journal of Tribology* 1989; 111(1): 136-141.
13. White J. A Gas Lubrication Equation for High Knudsen Number Flows and Striated Rough Surfaces. *Journal of Tribology* 2010; 132(2). 021701doi: 10.1115/1.4001023
14. Patir N, Cheng H. Application of Average Flow Model to Lubrication Between Rough Sliding Surfaces. *Journal of Lubrication Technology* 1979; 101(2): 220-230.
15. Patir N, Cheng H. An Average Flow Model for Determining Effects of Three-Dimensional Roughness on Partial Hydrodynamic Lubrication. *Journal of Lubrication Technology* 1978; 100(1): 12-17.
16. Li WL, Weng CI. Modified average Reynolds equation for ultra-thin film gas lubrication considering roughness orientations at arbitrary Knudsen numbers. *Wear* 1997; 209(1): 292 - 300. doi: https://doi.org/10.1016/S0043-1648(97)00019-7
17. Bayada G, Faure J. A Double Scale Analysis Approach of the Reynolds Roughness - Comments and Application to the Journal Bearing. *Journal of Tribology* 1989; 111(2): 323-330.

18. Buscaglia GC, Jai M. Homogenization of the Generalized Reynolds Equation for Ultra-Thin Gas Films and Its Resolution by FEM . *Journal of Tribology* 2004; 126(3): 547-552. doi: 10.1115/1.1739410

19. White J, Raad P. Effect of a rough translating surface on gas film lubrication: a numerical and analytical study. 1987.

20. Kuria I, Raad P. An Implicit Multidomain Spectral Collocation Method for the Simulation of Gas Bearings Between Textured Surfaces. *Journal of Tribology* 1996; 118(4): 783-793. doi: 10.1115/1.2831609

21. Wu Y, Yang L, Xu T, Xu H. Interactive effects of rarefaction and surface roughness on aerodynamic lubrication of microbearings. *Micromachines* 2019; 10(2): 155.

22. Brunetière N, Francisco A. Multiscale Modeling Applied to the Hydrodynamic Lubrication of Rough Surfaces for Computation Time Reduction. *Lubricants* 2018; 6(3): 83-12p. doi: 10.3390/lubricants6030083

23. Elrod H. A General Theory for Laminar Lubrication With Reynolds Roughness. *Journal of Lubrication Technology* 1979; 101(1): 8-14.

24. Brunetiere N. A General Model for Liquid and Gas Lubrication, Including Cavitation. *Journal of Tribology* 2018; 140: 021702-10p. doi: 10.1115/1.4037355

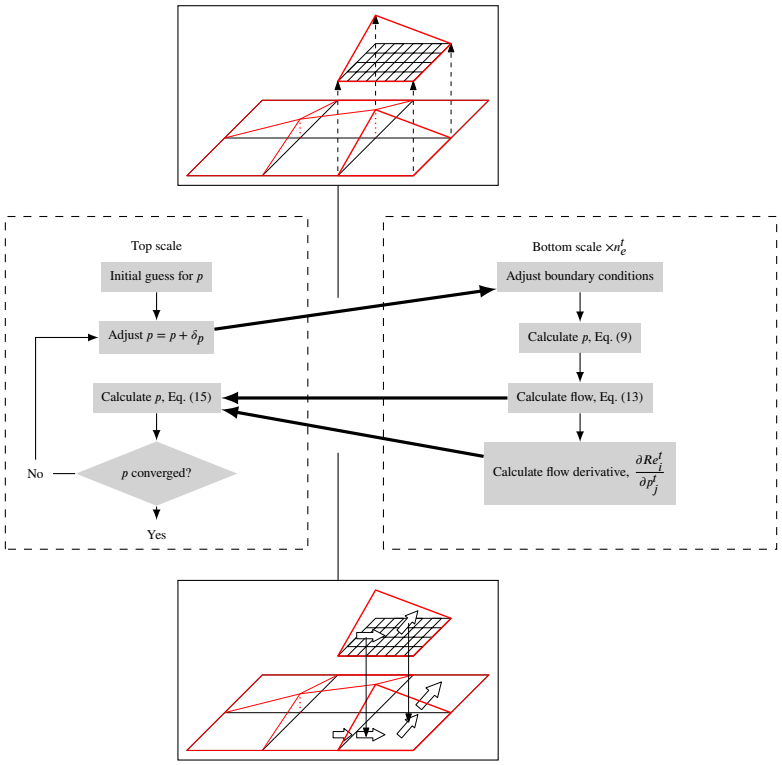

FIGURE 4 Multiscale solution procedure of MuSST.

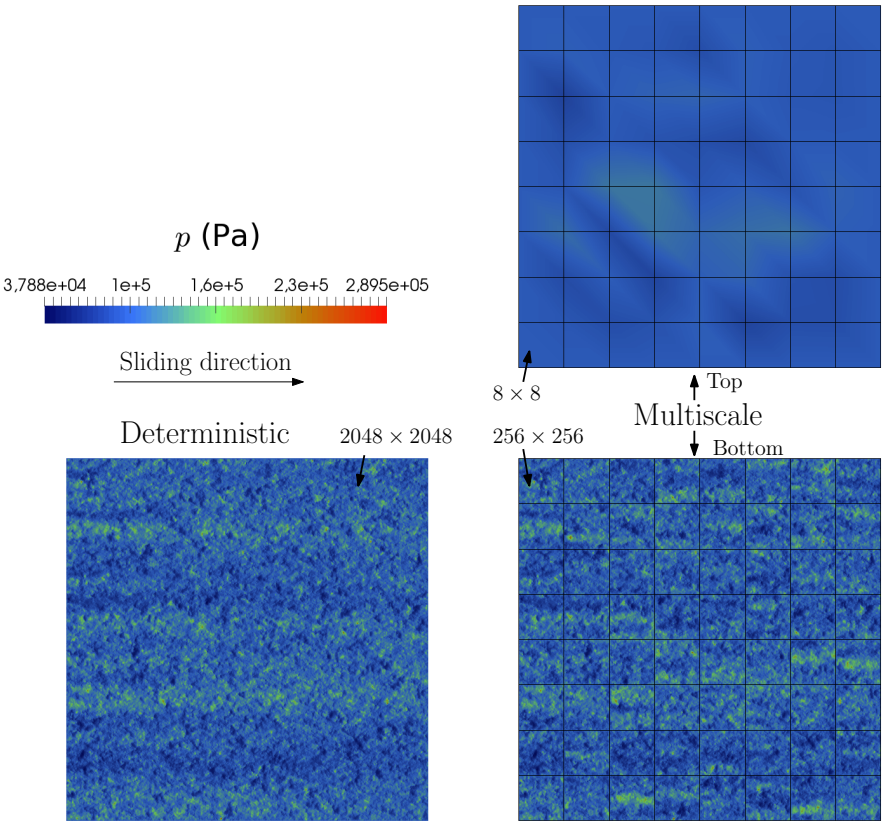

FIGURE 5 Example of results at $\Lambda = 1350$ with the reference rough surface. Pressure distributions obtained with the deterministic and multiscale approaches.

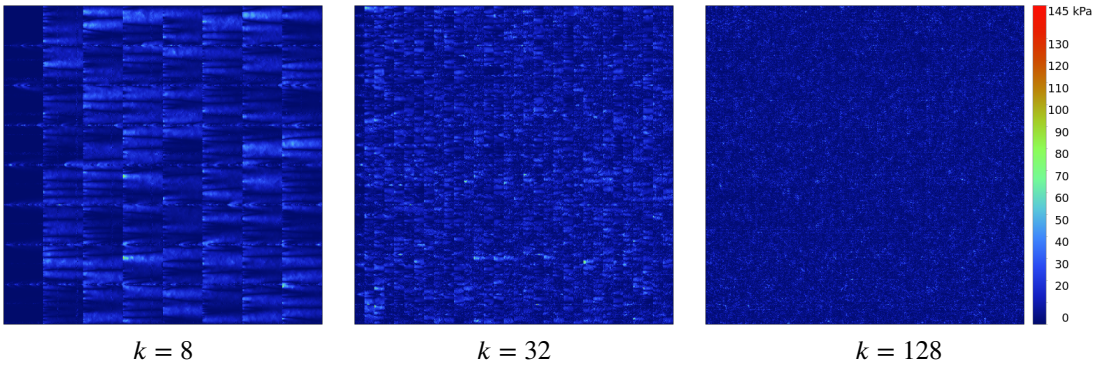

FIGURE 6 Absolute value of the pressure difference between the deterministic and multiscale solutions for different k at $\Lambda = 1350$ with the reference rough surface.

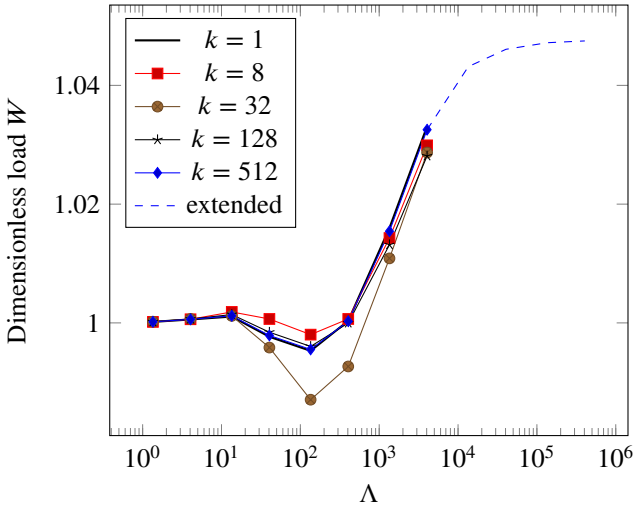

FIGURE 7 Calculated load as a function of the compressibilitty number.

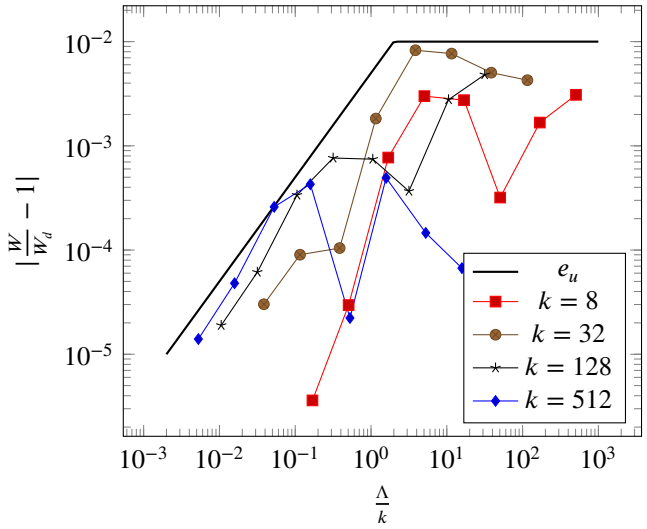

FIGURE 8 Error of the computed load as a function of the macro-compressibility number for different k

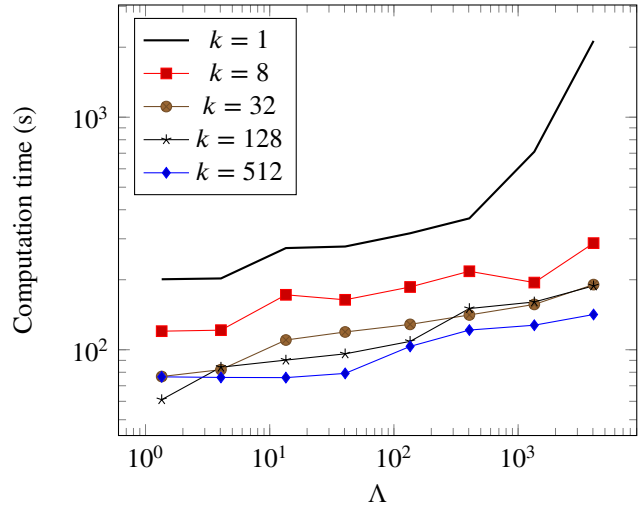

FIGURE 9 Computation time as a function of the compressibilitty number.

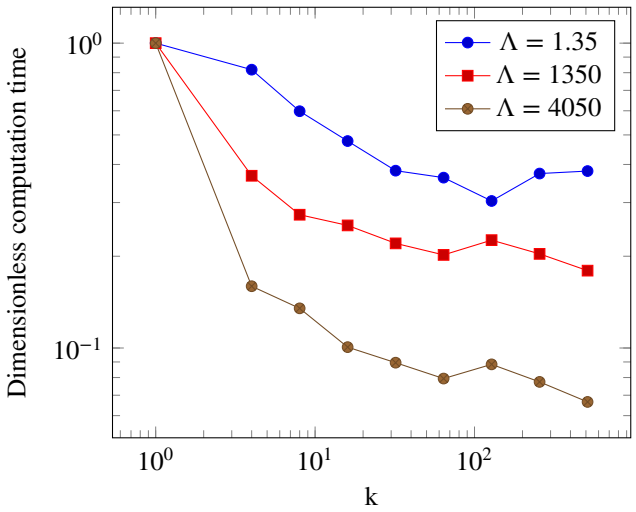

FIGURE 10 Computation time as a function of the number of subdomains per side k.

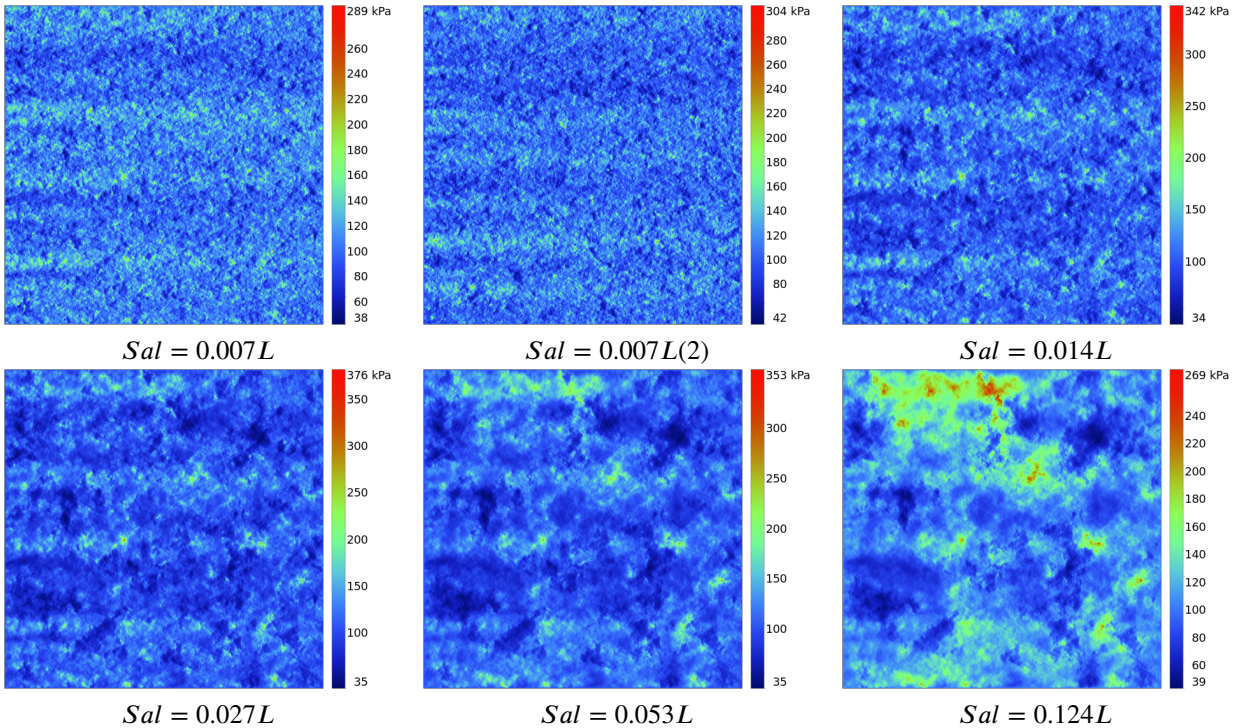

FIGURE 11 Pressure distribution obtained with the deterministic approach and the different surfaces for $\Lambda = 1350$. Sliding direction form left to right.

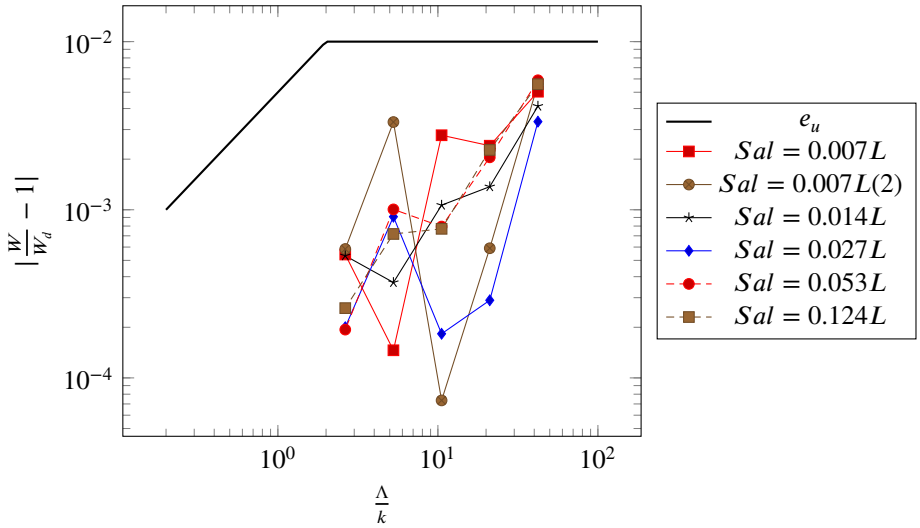

FIGURE 12 Error of the computed load as a function of the macro-compressibility number for different lateral sizes of the asperities

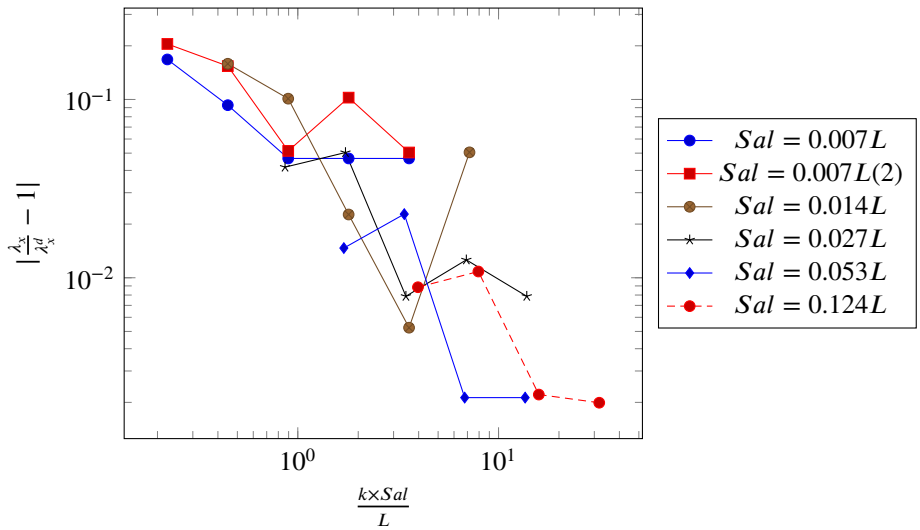

FIGURE 13 Error of the pressure correlation length in the sliding direction as a function of the ratio of the surface correlation length to the macro-element size for the different rough surfaces; $\Lambda = 1350$.

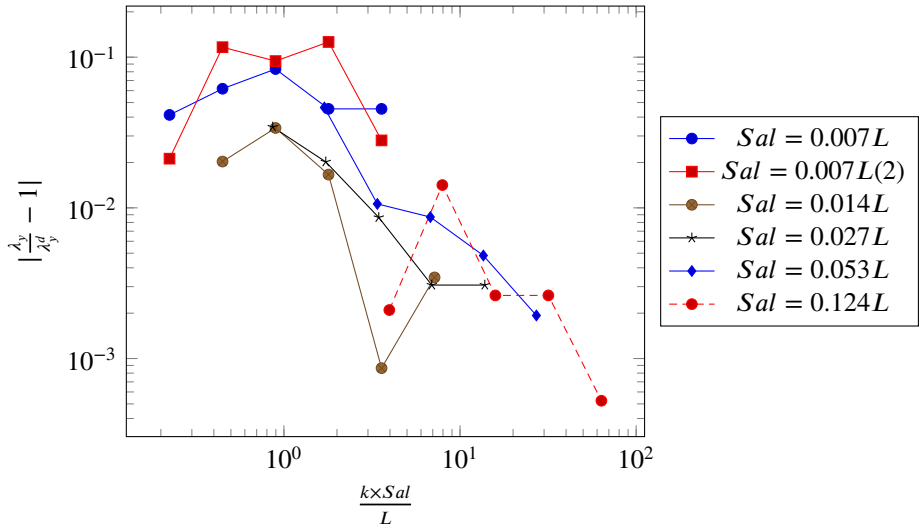

FIGURE 14 Error of the pressure correlation length in the y direction as a function of the ratio of the surface correlation length to macro-element size for the different rough surfaces; $\Lambda = 1350$.

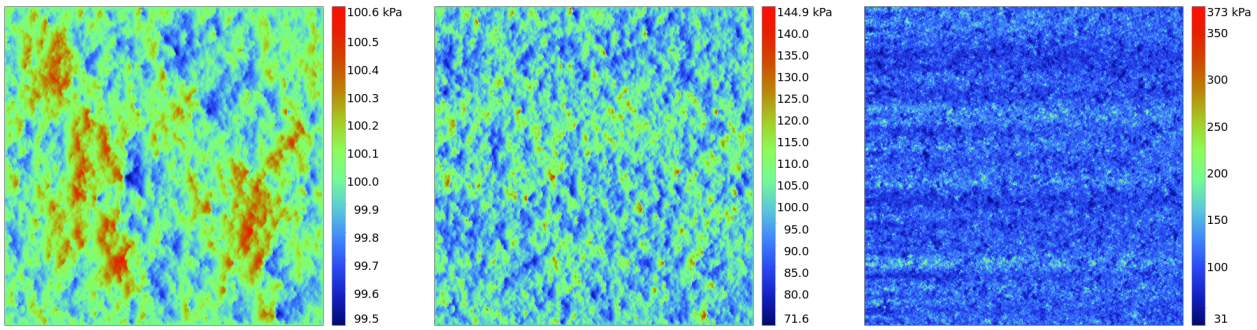

$\Lambda = 1.35$ $\Lambda = 135$ $\Lambda = 4050$

FIGURE 15 Pressure distribution obtained with the determinsitic approach and the refence surfaces for different values of the compressibility number Λ. Sliding direction form left to right.

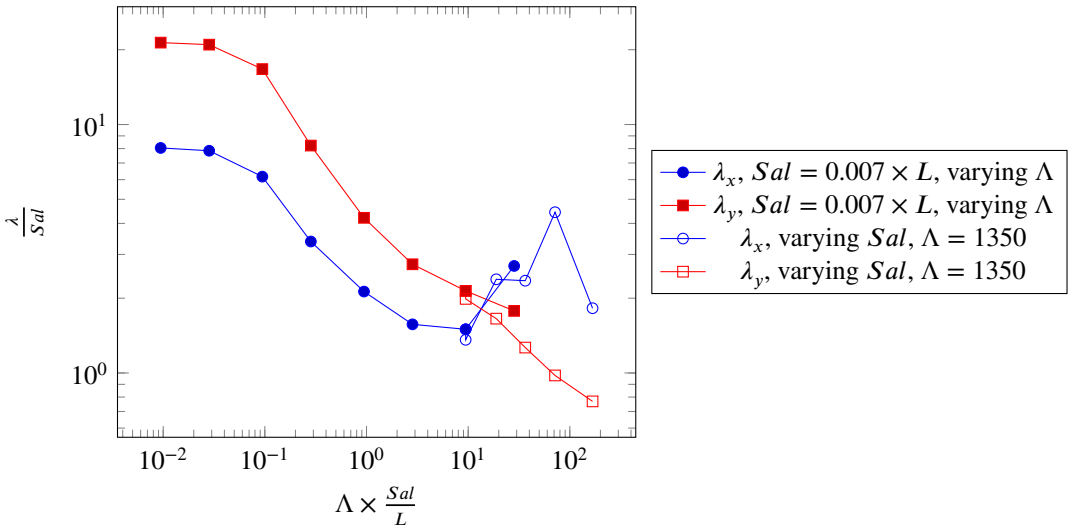

FIGURE 16 Correlation length of the pressure distribution in the x and y directions as a function of the compressibility number based on the roughness scale. Results obtained with the deterministic model.